

Unconventional electron states in δ -doped SmTiO_3

Frank Lechermann

*I. Institut für Theoretische Physik, Universität Hamburg, D-20355 Hamburg, Germany and
Institut für Keramische Hochleistungswerkstoffe, Technische Universität Hamburg-Harburg, D-21073 Hamburg, Germany*

The Mott-insulating distorted perovskite SmTiO_3 , doped with a single SrO layer in a quantum-well architecture is studied by the combination of density functional theory with dynamical mean-field theory. A rich correlated electronic structure in line with recent experimental investigations is revealed by the given realistic many-body approach to a large-unit-cell oxide heterostructure. Coexistence of conducting and Mott-insulating TiO_2 layers prone to magnetic order gives rise to multi-orbital electronic transport beyond standard Fermi-liquid theory. First hints towards a pseudogap opening due to electron-electron scattering within a background of ferromagnetic and antiferromagnetic fluctuations are detected.

Doped Mott insulators pose a challenging condensed matter problem (see e.g. [1] for a review). At stoichiometry, simple correlated metals show renormalized Landau-like quasiparticles, while charge-gapped Mott (including charge-transfer) insulators often reveal long-range order at low temperature with again a Landau-like order parameter. On the contrary, prominent materials such as e.g. high- T_c cuprates, double-exchange driven manganites or the correlated-spin-orbit iridate family prove that doping a Mott-insulating state can give rise to novel intricate phases, often beyond the Landau paradigm.

The in-depth experimental and theoretical analysis of the effect of random doping in bulk systems is usually hindered by the impact of disorder on introduced charges and local structural relaxations. This renders the definition of relevant length scales, e.g. screening distances, difficult. Due to the complexity of the problem, many theories of doped correlated materials, especially on the model-Hamiltonian level, neglect details of the local-chemistry aspect. But this may be insufficient to elucidate the subtle energy-scale balancing of strongly correlated electrons systems prone to long-range order.

Two developments are eligible to shed new light on this longstanding problem. First the rising field of oxide heterostructures allows experimentalists to introduce well-defined doping layers in correlated materials [2, 3]. Thereby the problem of disorder and ambiguities in identifying unique length scales are removed. Second the combination of first-principles density functional theory (DFT) with dynamical mean-field theory (DMFT) accounts for the interplay of bandstructure features and many-body effects beyond the realm of static-correlation approaches [4, 5]. Allying these progresses by addressing a doped-Mott-insulator heterostructure via DFT+DMFT is thus proper to reveal new insight into a hallmark challenge of interacting electrons.

The distorted perovskite SmTiO_3 as a member of the $R\text{TiO}_3$ (R : rare-earth element) series with formal Ti^{3+} - $3d(t_{2g}^1)$ configuration is Mott-insulating at stoichiometry. It displays antiferromagnetic (AFM) ordering below $T_N = 45\text{K}$. Notably, in the given $3d^1$ titanate series the compound is just at the border of a quantum-critical

transformation from antiferromagnetic to ferromagnetic (FM) order [6]. Recent experimental work focusing on δ -doping SmTiO_3 by a single SrO layer exposed non-Fermi-liquid (NFL) character, with a subtle crossover to still intriguing transport behavior when adding further doping layers [7–9].

In this work, a realistic many-body approach is employed to resolve the multi-orbital correlated electronic structure of δ -doped SmTiO_3 . We reveal a coexistence between itinerant and Mott-insulating real-space regions associated with different orbital polarizations. Non-Fermi-liquid behavior originates from the internal boundaries. Eventually, the scattering of itinerant carriers with spin fluctuations near the designed AFM-FM crossover is responsible for a pseudogap fingerprint, giving reason for the realistic NFL regime. These findings pave the way for theoretical investigations of oxide interfaces conducted by materials-design approaches beyond the possibilities of static mean-field studies.

Charge self-consistent DFT+DMFT [10–12] is used to access the many-body correlated electronic structure, using a correlated subspace composed of effective (i.e. Wannier-like) [13–16] Ti $3d(t_{2g})$ orbitals $w(t_{2g})$ [17]. Local Coulomb interactions in Slater-Kanamori form are parametrized by a Hubbard $U = 5\text{eV}$ and a Hund's coupling $J_H = 0.64\text{eV}$ [18]. The multi single-site DMFT impurity problems [19] are solved by the continuous-time quantum Monte Carlo scheme [20–23].

Let us focus first on stoichiometric SmTiO_3 (cf. Fig. 1a). Besides the lattice parameters, characteristic for the GdFeO_3 -type distorted-perovskite structure (space group $Pbnm$) are the Ti-O(1,2)-Ti bond angles, whereby O1(2) is the apical(basal in-plane) oxygen position with respect to the c -axis [6]. In bulk SmTiO_3 , these angles read $\varphi_1, \varphi_2 = 146^\circ, 147^\circ$. Based on the experimental crystal data [6], the $\text{Ti}(t_{2g})$ states form an isolated low-energy metallic band manifold of width $W \sim 1.55\text{eV}$ in DFT. A small orbital polarization towards an nearly isotropic effective t_{2g} state $|2\rangle = 0.58|xz\rangle + 0.53|yz\rangle + 0.62|xy\rangle$ is detected. The remaining two effective t_{2g} orbitals are given by $|1\rangle = 0.76|xz\rangle - 0.63|yz\rangle - 0.17|xy\rangle$ and $|3\rangle = 0.30|xz\rangle + 0.57|yz\rangle - 0.78|xy\rangle$. In line with ex-

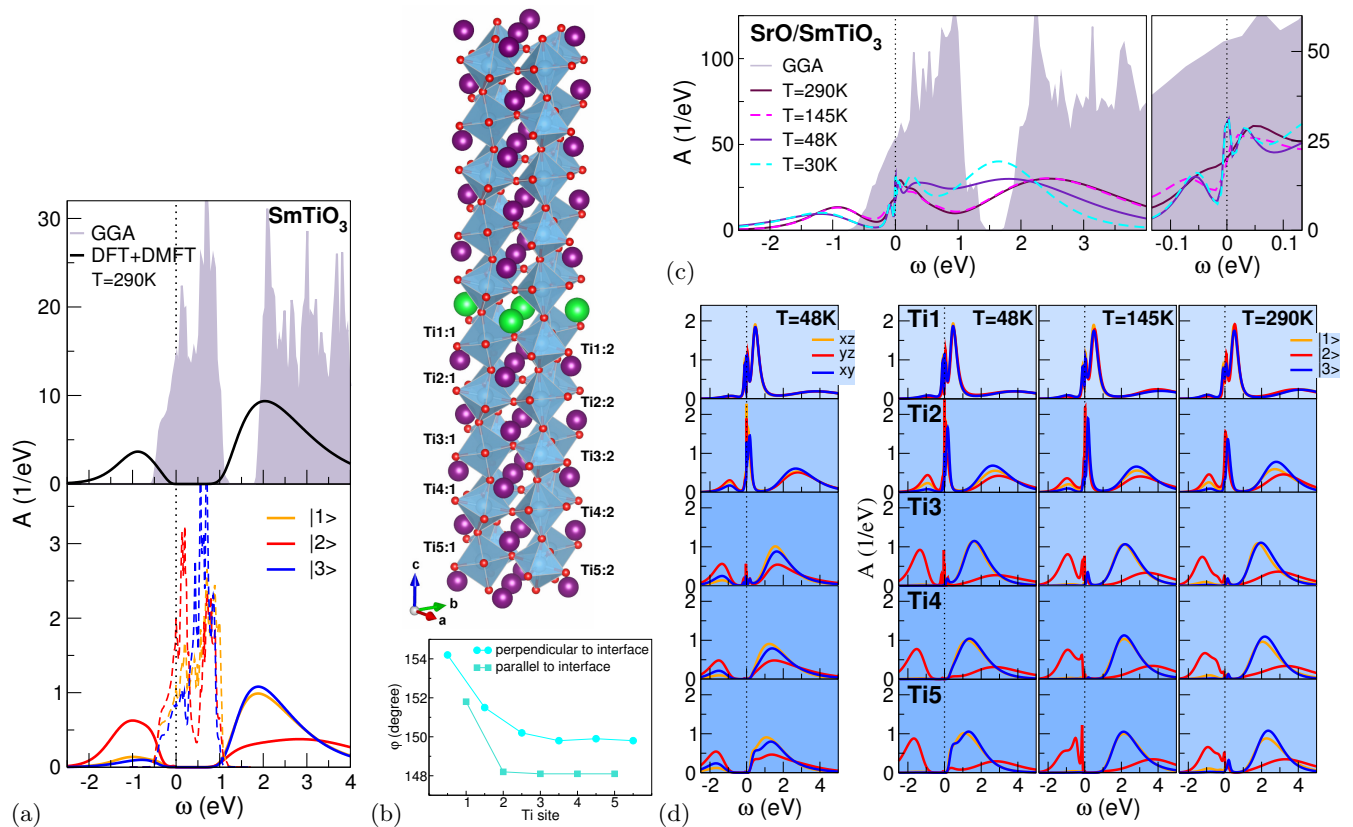


FIG. 1. (color online) DFT+DMFT results for paramagnetic undoped/ δ -doped SmTiO_3 . (a) Correlated electronic structure of stoichiometric SmTiO_3 . (b) Top: supercell of the δ -doped compound: Sm (violet), Sr (green), Ti (lightblue), O (small red), bottom: Ti-O-Ti bond angles. (c,d) Spectral function of the δ -doped system for (c) the total system and (d) Ti-resolved, left: for a single temperature in the conventional cubic t_{2g} basis and right: over a wider T range in the symmetry-adapted Ti-dependent effective t_{2g} basis.

periment, strong electron correlations drive the material paramagnetic (PM) Mott insulating by effectively localizing a single t_{2g} electron on the Ti site. Furthermore, as observed in theoretical assessments of other Mott-insulating $3d^1$ titanates [18, 24, 25], a substantial orbital polarization, here towards state $|2\rangle$, occurs. The orbital occupation reads $(n_1, n_2, n_3) = (0.15, 0.75, 0.10)$. If we define the charge gap Δ_g by spectral weight $< 10^{-4} \text{ eV}^{-1}$, a value $\Delta_g = 0.55 \text{ eV}$ is obtained, in good agreement with the mid-infrared-absorption onset of 0.50 eV [26]. Below its Néel temperature, bulk SmTiO_3 becomes an G-type antiferromagnet in experiment. Calculations show [17] that still various magnetic orderings are nearly degenerate in energy, in line with the system being on the verge to an AFM-FM transition.

Our 100-atom-unit-cell superlattice establishes δ -doping of SmTiO_3 by a single SrO layer [17]. It incorporates five symmetry-inequivalent TiO_2 layers each with two lateral inequivalent Ti sites (see Fig. 1b). The Mott insulator is doped with two holes, i.e. nominally 0.1 hole per Ti. In the experimental setting of Ref. [7, 8] the original c -axis is *parallel* to SrO and the original a, b -axes are inclined. To account for this fact approximatively,

we bring the original lattice parameters [6] in the same directional form, but without lowering the $Pbnm$ symmetry and relax all atomic positions. At the doping layer the bond angles $\varphi_{1,2}$ are enhanced (see Fig. 1b). There the system is structurally driven towards cubic SrTiO_3 . As expected, beyond 3-4 layers the characteristic angles saturate to bulk-like values [27]. Not-surprisingly, this saturation happens faster in terms of layers for the in-plane angle, since the out-of-plane φ_1 is stronger affected from a plane-parallel interface.

The PM many-body electronic structure upon δ -doping is exhibited in Figs. 1c,d. In line with experimental findings [7], DFT+DMFT reveals metallicity, but with characteristics different from GGA. The total spectral function $A(\omega)$ shows strong band narrowing and transfer of spectral weight to Hubbard bands. These processes depend rather significantly on the temperature T . Already for $T = 145 \text{ K}$ an obvious spectral reduction sets in at low-energy. This means that the coherence scale for low-energy excitations is far more lower than in many other correlated bulk systems. Comparison between $T = 48 \text{ K}, 30 \text{ K}$ data shows that the overall electronic structure finally settles well below the coherence scale, giving

rise to a lower Hubbard band at around -1.2eV . Notably within a small $[-0.1, 0.1]\text{eV}$ energy window around the Fermi level, a three-peak quasiparticle (QP)-like structure emerges. It should not be confused with the conventional large-energy-range three-peak structure involving lower and upper Hubbard bands.

We did not encounter intra- or inter-layer charge-ordering instabilities. Such charge ordering could even not be meta-stabilized. Especially the in-plane Ti ions behave equivalent, thus no need for intra-layer differentiation in the discussion. However the correlated subspace of $w(t_{2g})$ orbitals becomes layer-Ti dependent. Still, the Wannier-like functions in the different layers group again in the bulk-established subclasses, and the notion of $w(t_{2g}) = |1\rangle, |2\rangle, |3\rangle$ orbitals in each layer remains coherently applicable.

Different electronic phases are detected with distance to the SrO doping layer (see Fig. 1d). While the nearest TiO₂ layer is orbital-balanced conducting, the layers beyond the second one become strongly orbital-polarized Mott insulating at low T . The second layer itself is metallic, however displays strong correlations with already substantial orbital $|2\rangle$ polarization. With raising temperature, the more distant layers partly also obtain metallic character, but in a very incoherent fashion without clear QP formation. The orbital occupations only weakly depend on T but have strong layer dependence (see Tab. I). As in the bulk, layers 3-5 localize one electron in the Ti(t_{2g}) shell, whereas the 2nd layer with about 0.9 electrons is in a doped-Mott state. The first layer with 0.6 electrons appears as a renormalized metal. Hence between different TiO₂ layers, intricate metal-insulator transitions with strong orbital signature and delicate T dependence below room temperature are revealed.

For the rest of the paper, we refer to the nearest(next-nearest) TiO₂ plane with respect to the SrO doping plane as 'first(second) layer'. In order to assess the transport characteristics of these two conducting layers, the low-frequency behavior of the respective orbital-resolved self-energies $\Sigma(i\omega_n)$ is analyzed in Fig. 2 [17]. Assuming an overall Fermi-liquid regime, the QP weight $Z = (1 - \frac{\partial \text{Im} \Sigma(i\omega_n)}{\partial \omega_n} |_{\omega_n \rightarrow 0^+})^{-1} = \frac{m_{\text{GGA}}^*}{m^*}$ and the electron-electron scattering rate $\beta\Gamma = -\beta Z \text{Im} \Sigma(i0^+)$ is displayed, whereby m^* denotes the effective mass and $\beta =$

orbital	Ti1	Ti2	Ti3	Ti4	Ti5
$ 1\rangle$	0.22	0.29	0.05	0.04	0.04
$ 2\rangle$	0.16	0.48	0.94	0.95	0.95
$ 3\rangle$	0.24	0.12	0.01	0.01	0.01
sum	0.62	0.89	1.00	1.00	1.00

TABLE I. Temperature-averaged effective Ti(t_{2g}) occupations within each TiO₂ layer of δ -doped SmTiO₃.

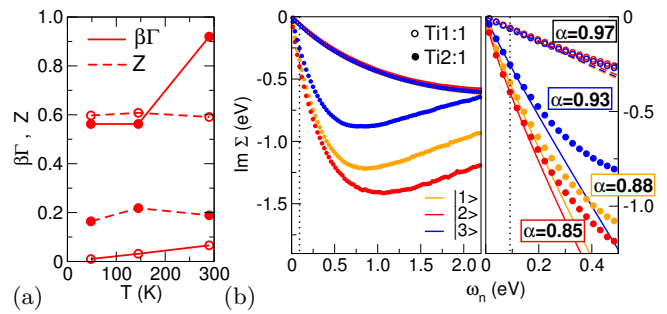


FIG. 2. (color online) Transport analysis for both conducting layers. (a) QP weight and scattering rate for the $|2\rangle$ state. (b) Orbital-resolved imaginary part of the self-energy on the Matsubara axis $\omega_n = (2n + 1)\pi T$. Left: larger frequency range, right: low-frequency region with fitting functions $\text{Im} \Sigma(\omega_n) = C_0 + A\omega_n^\alpha$ (dashed/full lines). Exponential-fitting cutoff n_c is denoted by the dotted line [17].

$1/T$. Whereas the first layer indeed shows well-developed Fermi-liquid like scattering and moderate $Z_1 \sim 0.6$, the second layer inherits strong scattering and a much smaller formal $Z_2 \sim 0.2$. To examine the quality of the Fermi-liquid character, an exponential-function fit is performed to the imaginary part of $\Sigma(i\omega_n)$, i.e. $\text{Im} \Sigma(\omega_n) \stackrel{!}{=} C_0 + A\omega_n^\alpha$ [28]. An ideal exponent $\alpha = 1$ marks a well-defined Fermi liquid with corresponding T^2 -law for the resistivity. Here indeed Fermi-liquid-like values $\alpha_1 = 0.97$ and $C_0 \rightarrow 0$ are extracted for the first layer, but for the dominant orbital $|2\rangle$ in the second layer an exponent $\alpha_2 = 0.85$ and finite intercept $C_0 \sim -0.01\text{eV}$ are obtained. Thus the second layer, mediating between Fermi-liquid and Mott-insulator, is put into a non-Fermi-liquid regime. This happens when the overall coherence scale is already reached, hence a conventional bad-metal picturing is not easily applicable. Note that in experiment, also a subtle NFL regime with $T^{5/3}$ -law is measured for δ -doped SmTiO₃ [7].

To shed further light onto the nature of the NFL behavior, possible broken-symmetry states are taken into account. Albeit various initializing starting points are investigated, again (spin-broken-assisted) charge-ordering instabilities are not supported by the present theoretical schemes. On the other hand, A-type AFM ordering, i.e. intra-layer FM and inter-layer AFM order, is readily a solution on the GGA level. Starting therefrom, DFT+DMFT quickly converges towards the same-kind many-body A-AFM phase at low temperatures (see Fig. 3a,b). Note that this is not a strict bulk-like A-AFM ordering, but the opposite Ti1 layers sandwiching SrO have identical FM direction with comparatively small magnetic moment. In addition, both Ti5 layers at the respective cell boundary are also FM aligned.

There is strongly reduced total spectral weight at the Fermi level compared to GGA, but the first layer exhibits spin-polarized QP-like peaks at ϵ_F associated with

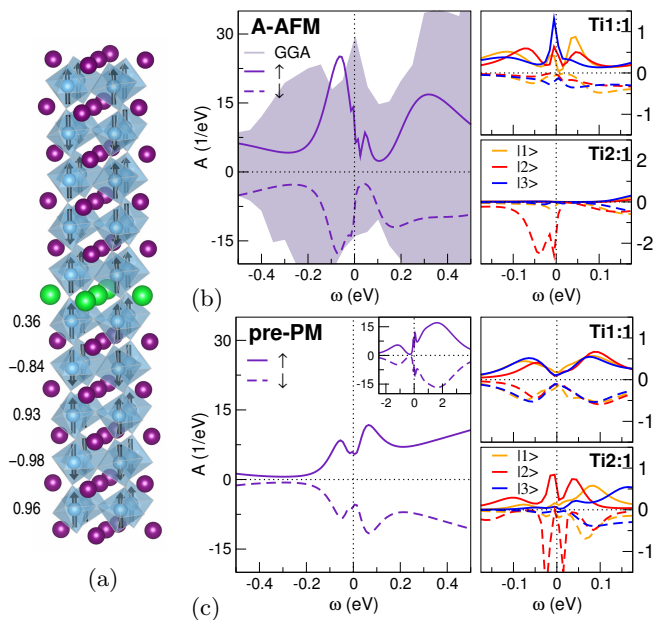


FIG. 3. (color online) δ -doped SmTiO_3 with broken spin symmetry ($T = 48\text{K}$). (a) A-AFM magnetic order, numbers provide local Ti magnetic moment in μ_B . (b,c) Spectral function, left: total, right: local Ti for first and second layer (similar data for Ti:2 sites). (b) A-type AFM phase. (c) pre-converged phase (after 20 DFT+DMFT steps), when starting the self-consistent calculation from the PM solution.

an Fermi-liquid-like exponent $\alpha = 0.95$. The delicate second FM layer is again strongly orbital- as well as spin-polarized, and notably already insulating. Intra-layer (or G-type) AFM ordering is not a strong competitor, although various starting points and mixing schemes were applied to stabilize such a metastable solution. Yet the introduced hole doping should indeed weaken the effective (because of strong orbital polarization) half-filled strong-AFM scenario in favor of FM tendencies. Thus part-FM order, especially close to the doping layer and for SmTiO_3 , is not that surprising.

An important observation is made, which delivers information concerning the many-body fluctuations: when starting from the previous PM solution and allowing for spin polarization, DFT+DMFT converges back to the original PM phase via an intriguing intermediate pseudogap state (cf. Fig 3c). The prominent pseudogap signature $\Delta_{\text{PG}} \sim 0.1\text{eV}$ appears after about 15 self-consistency steps and is quasi-stable for many further calculational steps. Therein, local moments are rather small, i.e. $m(\text{Ti1-5}) = (0.0, -0.02, 0.01, 0.09, 0.04) \mu_B$. Interestingly, the pseudogap is associated with orbital- and spin-balanced electron characteristics in the first layer. The parameters C_0 and α are still Fermi-liquid-like in that layer. Yet for Ti2 especially the intercept is rather large with $C_0 \sim -0.25\text{eV}$ in the pseudogap state. This underlines the strong NFL electron-electron scattering in the second layer.

Hence the electronic states attached to SrO are rather fragile and strongly affected by fluctuations around the PM solution. Due to the dominant magnetic instability in δ -doped SmTiO_3 , the pseudogap fingerprint in an intermediate state is interpreted to originate from the proximity to the AFM-to-FM instability. Scattering of first-layer itinerant electrons at emerging moments in the deeper layers below causes a significant spectral-weight reduction at ε_F . Two older perspectives are worth mentioning in this context. Non-Fermi-liquid behavior has been observed in DMFT calculations for a two-orbital Hubbard model due to double-exchange physics induced by orbital selectivity [29]. Seemingly there are some similarities with the present findings, though the two-orbital scenario is here replaced by an effective two-layer scenario. In view of the experimental $T^{5/3}$ -law for the resistivity, such an exponent is obtained for a metal prone to ferromagnetism [30] and was e.g. discussed in the context of Ni_3Al [31]. This may underline the relevance of additional FM fluctuations in the present AFM-based system.

An emerging pseudogap in few-layer SrO-doped SmTiO_3 is indeed reported in recent tunneling-spectroscopy experiments [32]. Pseudogap behavior is well known for the twodimensional one-band Hubbard model proximate to AFM order [33–37], described beyond single-site DMFT. But here, intriguing intra/inter-layer-resolved self-energies are sufficient to provide a multi-orbital fingerprint of such a fluctuation-dominated phase in the pre-converged DFT+DMFT cycle. Full stabilization of a pseudogap phase would ask for inter-site self-energies in the theoretical description. However note that the present pseudogap fingerprint does not emerge from sole in-plane correlations *parallel* to the interface, but additionally from perpendicular-to-interface correlations. This may create room for novel designing options of this fluctuation physics in terms of different layering/spacing.

To summarize, we find layer-dependent multi-orbital metal-insulator transitions in δ -doped SmTiO_3 with delicate temperature dependence. Unconventional metallicity for the two TiO_2 layers close to the SrO doping layer is revealed and nearly completely orbital-polarized Mott-insulating layers beyond. The next-nearest TiO_2 layer is critical in the sense that it mediates between the Fermi-liquid layer and the Mott layers, resulting in NFL behavior in line with experimental findings. This NFL regime is associated with strong AFM-to-FM spin fluctuations that may lead to a pseudogap structure at the Fermi level. Finally, the present many-body oxide-heterostructure study shall stimulate the investigation of novel emergent electronic phases [38, 39] by advanced theoretical means on the realistic level.

The author is indebted to S. Stemmer for helpful discussions. This research was supported by the Deutsche Forschungsgemeinschaft through FOR1346. Computations were performed at the University of Hamburg and

the JURECA Cluster of the Jülich Supercomputing Centre (JSC) under project number hhh08.

-
- [1] M. Imada, A. Fujimori, and Y. Tokura, *Rev. Mod. Phys.* **70**, 1039 (1998).
- [2] J. N. Eckstein and I. Bozovic, *Annu. Rev. Mater. Sci.* **25**, 679 (1995).
- [3] S. Stemmer and A. J. Millis, *MRS Bulletin* **38**, 1032 (2013).
- [4] V. I. Anisimov, A. I. Poteryaev, M. A. Korotin, A. O. Anokhin, and G. Kotliar, *J. Phys.: Condens. Matter* **9**, 7359 (1997).
- [5] A. I. Lichtenstein and M. Katsnelson, *Phys. Rev. B* **57**, 6884 (1998).
- [6] A. C. Komarek, H. Roth, M. Cwik, W.-D. Stein, J. Baier, M. Kriener, F. Bourée, T. Lorenz, and M. Braden, *Phys. Rev. B* **75**, 224402 (2007).
- [7] C. A. Jackson, J. Y. Zhang, C. R. Freeze, and S. Stemmer, *Nat. Commun.* **5**, 4258 (2014).
- [8] E. Mikheev, C. R. Freeze, B. J. Isaac, T. A. Cain, and S. Stemmer, *Phys. Rev. B* **91**, 165125 (2015).
- [9] E. Mikheev, S. Raghavan, J. Y. Zhang, P. B. Marshall, A. P. Kajdos, L. Balents, and S. Stemmer, *Sci. Rep.* **6**, 20865 (2016).
- [10] S. Y. Savrasov, G. Kotliar, and E. Abrahams, *Nature* **410**, 793 (2001).
- [11] L. V. Pourovskii, B. Amadon, S. Biermann, and A. Georges, *Phys. Rev. B* **76**, 235101 (2007).
- [12] D. Grieger, C. Piefke, O. E. Peil, and F. Lechermann, *Phys. Rev. B* **86**, 155121 (2012).
- [13] B. Amadon, F. Lechermann, A. Georges, F. Jollet, T. O. Wehling, and A. I. Lichtenstein, *Phys. Rev. B* **77**, 205112 (2008).
- [14] V. I. Anisimov, D. E. Kondakov, A. V. Kozhevnikov, I. A. Nekrasov, Z. V. Pchelkina, J. W. Allen, S.-K. Mo, H.-D. Kim, P. Metcalf, S. Suga, et al., *Phys. Rev. B* **71**, 125119 (2005).
- [15] M. Aichhorn, L. Pourovskii, V. Vildosola, M. Ferrero, O. Parcollet, T. Miyake, A. Georges, and S. Biermann, *Phys. Rev. B* **80**, 085101 (2009).
- [16] K. Haule, C.-H. Yee, and K. Kim, *Phys. Rev. B* **81**, 195107 (2010).
- [17] See supplementary material for further details.
- [18] E. Pavarini, S. Biermann, A. Poteryaev, A. I. Lichtenstein, A. Georges, and O. K. Andersen, *Phys. Rev. Lett.* **92**, 176403 (2004).
- [19] M. Potthoff and W. Nolting, *Phys. Rev. B* **59**, 2549 (1999).
- [20] A. N. Rubtsov, V. V. Savkin, and A. I. Lichtenstein, *Phys. Rev. B* **72**, 035122 (2005).
- [21] P. Werner, A. Comanac, L. de' Medici, M. Troyer, and A. J. Millis, *Phys. Rev. Lett.* **97**, 076405 (2006).
- [22] O. Parcollet, M. Ferrero, T. Ayrál, H. Hafermann, I. Krivenko, L. Messio, and P. Seth, *Comput. Phys. Commun.* **196**, 398 (2015).
- [23] P. Seth, I. Krivenko, M. Ferrero, and O. Parcollet, *Comput. Phys. Commun.* **200**, 274 (2016).
- [24] E. Pavarini, A. Yamasaki, J. Nuss, and O. K. Andersen, *New J. Phys.* **7**, 188 (2005).
- [25] F. Lechermann and M. Obermeyer, *New J. Phys.* **17**, 043026 (2015).
- [26] D. A. Crandles, T. Timusk, J. D. Garrett, and J. E. Greedan, *Physica C* **201**, 407 (1992).
- [27] R. Chen, S. B. Lee, and L. Balents, *Phys. Rev. B* **87**, 161119(R) (2013).
- [28] P. Werner, E. Gull, M. Troyer, and A. J. Millis, *Phys. Rev. Lett.* **101**, 166405 (2008).
- [29] S. Biermann, L. de' Medici, and A. Georges, *Phys. Rev. Lett.* **95**, 206401 (2005).
- [30] J. Mathon, *Proc. R. Soc. London, Ser. A* **306**, 355 (1968).
- [31] P. G. Niklowitz, F. Beckers, G. G. Lonzarich, G. Knebel, B. Salce, J. Thomasson, N. Bernhoeft, D. Braithwaite, and J. Flouquet, *Phys. Rev. B* **72**, 024424 (2005).
- [32] P. B. Marshall, E. Mikheev, S. Raghavan, and S. Stemmer, *Phys. Rev. Lett.* **117**, 046402 (2016).
- [33] J. J. Deisz, D. W. Hess, and J. W. Serene, *Phys. Rev. Lett.* **76**, 1312 (1996).
- [34] C. Huscroft, M. Jarrell, T. Maier, S. Moukouri, and A. N. Tahvildarzadeh, *Phys. Rev. Lett.* **86**, 139 (2001).
- [35] B. Kyung, S. S. Kancharla, D. Sénéchal, A.-M. S. Tremblay, M. Civelli, and G. Kotliar, *Phys. Rev. B* **73**, 165114 (2006).
- [36] A. N. Rubtsov, M. I. Katsnelson, A. I. Lichtenstein, and A. Georges, *Phys. Rev. B* **79**, 045133 (2009).
- [37] A. A. Katanin, A. Toschi, and K. Held, *Phys. Rev. B* **80**, 075104 (2009).
- [38] Q.-Y. Wang, Z. Li, W.-H. Zhang, Z.-C. Zhang, J.-S. Zhang, W. Li, H. Ding, Y.-B. Ou, P. Deng, K. Chang, et al., *Chinese Phys. Lett.* **29**, 037402 (2012).
- [39] Y. Cao, Z. Yang, M. Kareev, X. Liu, D. Meyers, S. Middey, D. Choudhury, P. Shafer, J. Guo, J. W. Freeland, et al., *Phys. Rev. Lett.* **116**, 076802 (2016).
- [40] S. G. Louie, K. M. Ho, and M. L. Cohen, *Phys. Rev. B* **19**, 1774 (1979).
- [41] B. Meyer, C. Elsässer, F. Lechermann, and M. Fähnle, *Fortran 90 program for mixed-basis-pseudopotential calculations for crystals*.
- [42] J. P. Perdew, K. Burke, and M. Ernzerhof, *Phys. Rev. Lett.* **77**, 3865 (1996).
- [43] V. I. Anisimov, I. V. Solovyev, M. A. Korotin, M. T. Czyżyk, and G. A. Sawatzky, *Phys. Rev. B* **48**, 16929 (1993).

Supplemental Information

DFT+DMFT APPROACH

The charge self-consistent DFT+DMFT method is employed. For the DFT part, a mixed-basis pseudopotential method [40, 41] build on norm-conserving pseudopotentials as well as a combined basis of localized functions and plane waves. The generalized-gradient approximation (GGA) in the Perdew-Burke-Ernzerhof form [42], is put into practice. The partially-filled Sm($4f$) shell is treated in the frozen-core approximation since the highly-localized $4f$ electrons do not have key influence on the present doped-Mott physics. In the mixed-basis, localized functions are included for Ti($3d$) as well as for O($2s$), O($2p$) to reduce the energy cutoff E_{cut} for the plane waves.

Our correlated subspace consists of the effective Ti(t_{2g}) Wannier-like functions $w_n(t_{2g})$, i.e. is locally threefold. The $w(t_{2g})$ functions are obtained from the projected-local-orbital formalism [13–16], using as projection functions the linear combinations of atomic t_{2g} orbitals, diagonalizing the Ti $w_n(t_{2g})$ -orbital-density matrix. A band manifold of 60 t_{2g} -dominated Kohn-Sham states at lower energy are used to realize the projection. Local Coulomb interactions in Slater-Kanamori form for the $w_n(t_{2g})$ orbitals are parametrized by a Hubbard $U = 5\text{ eV}$ and a Hund's coupling $J_{\text{H}} = 0.64\text{ eV}$. These values for the local Coulomb interactions are common for correlated titanates [18]. The single-site DMFT impurity problems are solved by the continuous-time quantum Monte Carlo scheme [20, 21] as implemented in the TRIQS package [22, 23]. A double-counting correction of fully-localized type [43] is utilized. To obtain the spectral information, analytical continuation from Matsubara space via the maximum-entropy method is performed. About 40-50 DFT+DMFT iterations (of alternating Kohn-Sham and DMFT impurity steps) are necessary for full convergence.

MAGNETIC ORDER IN BULK SAMARIUM TITANATE

Bulk SmTiO₃ displays antiferromagnetic (AFM) order of G-type form below $T_{\text{N}} = 45\text{ K}$. Yet the compound is just at the border towards ferromagnetism, since already the next rare-earth titanate $R\text{TiO}_3$ (R : rare-earth element) in the given series, i.e. GdTiO₃, is ferromagnetic (FM). To provide insight into the subtle competition between different magnetic orders, we compute the total energies within GGA and GGA+U for the three most prominent AFM orderings, i.e. G-type, A-type and C-type as well as for FM ordering (see Fig. 4). A plane-wave energy cutoff $E_{\text{cut}} = 16\text{ Ryd}$ and a $9 \times 9 \times 9$ k -point grid

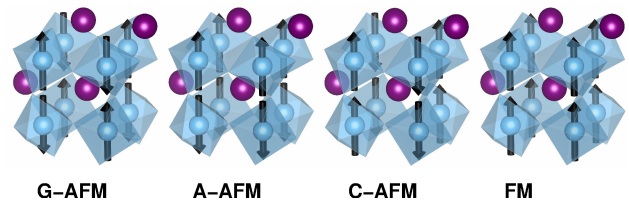


FIG. 4. Competing magnetic orders in SmTiO₃.

scheme	G-AFM	A-AFM	C-AFM	FM
GGA	11.3	2.1	10.8	0.0
	0.32	0.62	0.46	0.72
GGA+U	1.2	0.3	1.2	0.0
	0.73	0.75	0.74	0.76

TABLE II. Energy and magnetic moment for different magnetic orders in SmTiO₃. First line: energy E_{mag} (in meV/atom) of the magnetically ordered state with respect to the lowest energy in the given set. Second line: local Ti magnetic moment (in μ_{B}). For GGA+U, the values $U = 5\text{ eV}$ and $J_{\text{H}} = 0.64\text{ eV}$ are chosen.

is applied. The calculations are based on the 100 K experimental crystal data of Komarek *et al.* [6] and the resulting energies and Ti magnetic moments are displayed in Tab. II.

All ordering cases are at least metastable and the non-magnetic energy lies always higher, i.e. magnetic ordering is strongly favored at low temperatures. Note however that DFT(+U), in contrast to DFT+DMFT, does not allow to treat the true *paramagnetic* case. For each order, GGA(+U) yields metallic(insulating) solutions. The different ordered states are all very close in energy, at most they differ in about 10(1) meV/atom within GGA(+U). Albeit the numbers designate FM order as lowest, given the DFT approximation, especially for the Mott-insulating designed GGA+U an energy difference of 1 meV/atom is usually beyond the limit of physical significance. But the quasi-degeneracy of the magnetic orders is nonetheless physically sound, since as noted, SmTiO₃ is just at the AFM-to-FM transition point in the rare-earth titanate series.

STRUCTURAL DETAILS FOR THE δ -DOPED ARCHITECTURE

The δ -doped SmTiO₃ architecture is realized by a superlattice based on a 100-atom unit-cell. It consists of 10(9) TiO₂(SmO) layers, separated by a single SrO monolayer. Each TiO₂ layer is build from two possibly symmetry-inequivalent Ti ions, to allow for potential intra-layer spin or charge ordering. Together with the five-layer resolution away from the doping layer, there

are thus 10 inequivalent Ti single-site DMFT problems in our realistic modelling. The original lattice parameters [6] are brought in the directional form of the experimental works Ref. [7, 8], but without lowering the $Pbnm$ symmetry. The original c -axis is *parallel* to the doping layer and the original a, b -axes are respectively inclined. The plane-wave energy cutoff is set to $E_{\text{cut}} = 11$ Ryd and a $5 \times 5 \times 3$ k -point grid is used. With fixed lattice parameters, all atomic positions in the supercell are structurally relaxed within DFT(GGA) until the maximum individual atomic force settles below 5 mRyd/a.u.. The lattice distortion introduced by the SrO layer is well captured by the structural relaxations. No relaxation of the lattice parameters is performed. A change of lattice parameters is very small due to the structural similarity and does not invoke changes of the key physics discussed in the given work. The obtained crystal structure is used for the PM, A-AFM as well as the pre-converged electronic structure studies.

INFLUENCE OF THE LOCAL-INTERACTION STRENGTH

The chosen local Coulomb interactions are well established for bulk titanates [18]. A first-principles computation of these parameters for the large δ -doped architecture, including their layer dependence, is currently numerically unfeasible. In order to still examine the in-

fluence of smaller/larger local Coulomb interaction, we additionally studied the DFT+DMFT electronic structure for $U = 3.5$ eV and $U = 6.5$ eV. The Hund's exchange is even less sensitive and therefore remains fixed at $J_H = 0.64$ eV.

Figure 5 exhibits the layer-dependent Ti orbital filling with U . As expected, for the smaller value of U , the orbital polarization is much weaker for the layers beyond Ti1. Also the Mott state is not reached with distance from the doping layer up to Ti5, thus $U = 3.5$ eV appears too small to account for the correct δ -doping physics. On the other hand, for $U = 6.5$ eV the orbital polarization for Ti3-5 is even increased. Moreover, the second TiO₂ layer with Ti2 is also strongly orbital polarized for this larger U . The additionally shown Ti2 local spectral function in Fig. 5 reveals that the second layer is about to enter a Mott-insulating state. Hence a substantially larger, somewhat unphysical, Hubbard U destroys the two-layer dichotomy.

DETAILS ON THE SELF-ENERGY FITTING

The low-frequency characteristics of the local electronic self-energy within the two Ti layers closest to the SrO doping layer, i.e. Ti1 and Ti2, is analyzed in some detail in the main text. This allows to extract important information on the (non)-Fermi-liquid quality connected to states close to the Fermi energy. To assess this quality, we focus on two features of the self-energy, namely the intercept $C_0 = \lim_{\omega \rightarrow 0} \Sigma$ and the form $\tilde{Z}(\omega) = (1 - \frac{\partial \Sigma}{\partial \omega} |_{\omega \rightarrow 0})^{-1}$. For a Fermi liquid (FL) at low temperature, the intercept C_0 approaches zero and $\tilde{Z}(\omega) = Z$ is the constant quasiparticle (QP) weight. Significant deviations from these features signals a non-Fermi liquid (NFL).

We here provide further information on the self-energy fitting procedure in the δ -doped paramagnetic phase to enable such a discrimination, as well as on the grade of those fits. The relevant object in this context is the imaginary part of the Matsubara self-energy. In correct mathematical terms, this function reads $\text{Im} \Sigma(i\omega_n)$, with the fermionic Matsubara frequencies defined as $\omega_n = (2n + 1)\pi T$. From a sole fitting-function point of view, we however refer in the following to $\text{Im} \Sigma(\omega_n)$. Moreover we discuss the fitting parameters as dimensionless, imagining proper normalization.

Figure 6 shows different resolutions of the imaginary part of the multi-orbital self-energy with respect to the frequencies ω_n . The quantum-Monte-Carlo data is well converged at $T = 48$ K to facilitate our low-frequency examination. In order to check the influence on the frequency cutoff n_c (i.e. all frequencies with $n \leq n_c$ are used for the fit), different values for n_c are chosen. Two different stages of fitting procedures are performed and results are here exemplified for the dominant Ti |2> state

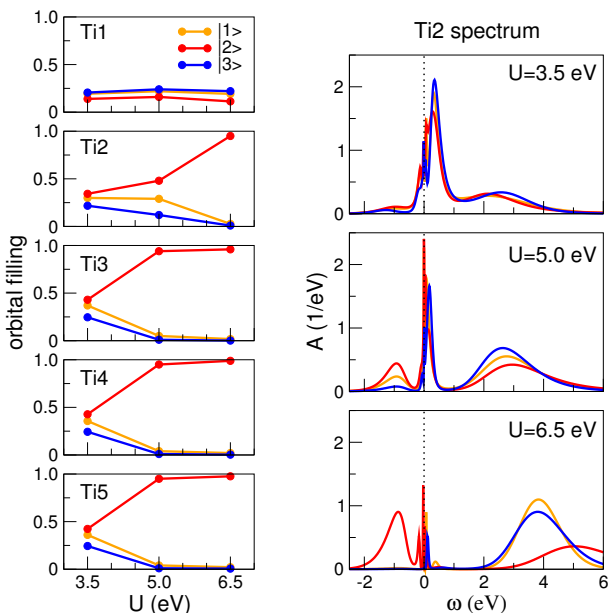


FIG. 5. (color online) Local Ti data for different values of Hubbard U and fixed $J_H = 0.64$ eV ($T = 48$ K). Left: layer-dependent paramagnetic orbital filling (with no difference between intra-layer Ti:1, Ti:2). Right: local Ti2 spectral function with respect to U .

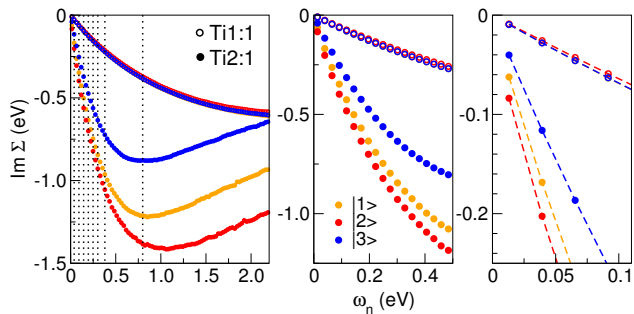


FIG. 6. (color online) Imaginary part of the Ti self-energy on the Matsubara axis for the first two TiO_2 layers with different resolution from left to right. Left: dotted lines mark the frequency cutoff $n_c = 2, 4, 6, 8, 10, 12, 16, 32$ in the different fits (see Tab. III). Dashed lines in right part are no fitting curves but guides to the eyes.

n_c	$\text{Im } \Sigma(\omega_n) = \sum_{k=0}^{1,5} a_k \omega_n^k$		$\text{Im } \Sigma(\omega_n) = C_0 + A \omega_n^\alpha$		
	$a_0 = C_0$	$(1 - a_1)^{-1} = Z$	C_0	A	α
2	-0.0006	0.61	—	—	—
4	-0.0006	0.61	$< 10^{-4}$	-0.61	0.98
6	-0.0016	0.66	$< 10^{-4}$	-0.58	0.96
8	-0.0009	0.63	$< 10^{-4}$	-0.56	0.94
10	-0.0009	0.63	$< 10^{-4}$	-0.54	0.93
12	-0.0004	0.61	$< 10^{-4}$	-0.53	0.92
16	$< 10^{-4}$	0.60	$< 10^{-4}$	-0.51	0.90
32	$< 10^{-4}$	0.60	0.0002	-0.62	0.98
2	-0.0243	0.18	—	—	—
4	-0.0382	0.20	-0.0131	-2.96	0.85
6	-0.0111	0.14	-0.0111	-2.68	0.81
8	-0.0171	0.16	-0.0084	-2.50	0.78
10	-0.0149	0.15	-0.0046	-2.36	0.75
12	-0.0177	0.16	$< 10^{-4}$	-2.25	0.72
16	-0.0189	0.16	$< 10^{-4}$	-2.11	0.69
32	-0.0267	0.17	$< 10^{-4}$	-2.69	0.80

TABLE III. Detailed results for the least-mean-squares fitting procedures applied to $\text{Im } \Sigma(\omega_n)$ in the δ -doped case, shown for the Ti $|2\rangle$ state in the first (top) and the second TiO_2 layer (bottom) next to the SrO doping layer. Left columns: polynomial fit, of first order for $n_c = 2 - 4$ and of fifth order for $n_c = 6 - 32$. Right columns: exponential fit for $n_c \geq 4$.

in the first (Ti1) and second (Ti2) layer next to SrO (see Tab. III). First, motivated by *assuming* Fermi-liquid theory holds, a polynomial fit of simplistic first order ($n_c \leq 4$) and of 5th order ($n_c \geq 6$) is processed. Intercept and Z are therefrom easily extracted from the zeroth and first-order terms, respectively. A good quality of the fitting shall focus on the very low-frequency region, but takes care of the ω_n evolution. Hence the sole linear fitting for very small n_c as well as the higher-order fit for rather large $n_c \sim 16 - 32$ are less suited to the problem. But the results show that a proper fitting leads to robust values for C_0 and Z with e.g. an error $\Delta Z \sim 0.03$.

Questioning Fermi-liquid behavior asks for an exponential fitting function with an exponent α (cf. Tab. III). Only for $\alpha = 1$ a constant QP weight and thus Fermi-liquid behavior is recovered. However the fitting is more exclusively restricted to small n_c . A large n_c results in a too small intercept C_0 , since the fitting function tries to account for the natural bending of $\text{Im } \Sigma(\omega_n)$ at larger ω_n by shifting C_0 towards zero. Still, the quality of our numerical data is high enough to reveal the resilient FL-to-NFL crossover from the first to the second TiO_2 layer. In the second layer, the exponent α manifestly deviates from unity and the intercept C_0 from zero. Hence electron-electron scattering is beyond FL theory and does not easily vanish at the Fermi energy. Of course the previous FL statements only fully hold for $T \rightarrow 0$, but our temperature is already well below a possible QP coherency scale and the contrasting behavior in the seemingly FL-like first TiO_2 layer is obvious.